Submitted to the Journal of Physical Oceanography for peer review, uploaded to EarthArXiv

Global distribution and governing dynamics of submesoscale density fronts

Caitlin B. Whalen[a] and Kyla Drushka[a]

[a] *Applied Physics Laboratory, University of Washington, Seattle, WA*

Corresponding author: Caitlin B. Whalen, cbwhalen@uw.edu

ABSTRACT: While the dynamics at submesoscales (0.1s-10s km) are thought to be important globally for a range of processes near the air-sea interface, few observational studies sufficiently span scales to include both the submesoscale and global scales, leaving many questions concerning the coupling between the scales unexplored. To address this gap, we use a global dataset of ship-based thermosalinograph and satellite sea surface temperature data to identify over a 250,000 submesoscale density fronts throughout the ocean. Globally, we find that the mean submesoscale frontal dynamics can be characterized by a scaling based on the assumption that the Rossby number and Froude number are proportional, $Ro \sim Fr$. Our results also show that the large-scale ocean characteristics play a role in setting the spatial variability of submesoscale frontal horizontal buoyancy gradients (i.e., frontal 'sharpness'). If the large-scale background density gradient is large and/or dominated by salinity as opposed to temperature variability, then submesoscale fronts tend to be sharper. We show that globally, shallow mixed layers are also associated with sharper submesoscale fronts, in contrast to previous regional-scale findings. This global perspective on the variability and dynamics of submesoscale fronts raises many additional questions and hopefully will inspire the formation of new scale-spanning avenues for future studies.

1. Introduction

Submesoscale density fronts (typically 0.1s-10s of km in width) play a critical role in a broad range of processes near the ocean's surface (McWilliams 2016; Taylor and Thompson 2023). Frontal dynamics at these scales contribute to the energy and buoyancy budgets in the upper ocean by generating strong vertical velocities and dissipating energy through turbulent mixing (e.g. D'Asaro et al. 2011; Thomas et al. 2013; Peng et al. 2020), as well as contributing to mixed layer restratification processes (e.g., Boccaletti et al. 2007). Vertical transport at these fronts has implications for the chemical and biological systems in the ocean including carbon export (Omand et al. 2015; Liu et al. 2018) and primary production (Mahadevan 2016). Due to the importance of submesoscale fronts at large scales, this study focuses on how large-scale ocean properties affect submesoscale density fronts globally.

Local processes are known to modulate the strength and evolution of submesoscale density fronts. For example, in an active mesoscale field, submesoscale fronts can be subject to mesoscale shear and strain, which can drive instabilities and sharpen the frontal gradients (Molemaker et al. 2005). In such a field, some fronts may also be aligned with the wind, forcing Ekman transport that sharpens or slumps the front (Thomas and Lee 2005; D'Asaro et al. 2011). Alternatively, a destabilizing surface buoyancy flux can drive processes that can produce submesoscale fronts through mixed layer baroclinic instability (Haine and Marshall 1998; Boccaletti et al. 2007), or sharpen existing fronts. Additionally, since tracers often have a shorter mixing timescale compared to the mixing of momentum (this set of assumptions is commonly called the subinertial mixed layer approximation, Young (1994)), density fronts tend to slump so that the observed salinity and temperature variability at submesoscales is driven toward density compensation (Rudnick and Ferrari 1999). The degree to which this process drives frontal compensation varies regionally (Spiro Jaeger and Mahadevan 2018; Drushka et al. 2019). Cumulatively, these local processes, and others, can alter the evolution of individual fronts and the characteristics of the local submesoscale field.

In contrast to local processes, less is understood about the interaction between submesoscale fronts and global-scale background properties due to the vast range of time and length scales involved. To address this challenge, studies have investigated the interactions between submesoscale fronts and the large scale by using two main approaches: (1) develop parameterizations based on the individual processes described above and then use models or observations to estimate their variability and impact, or (2) use regional or global submesoscale-permitting models as an approximation for a fully resolved submesoscale field. The first approach has yielded a number of advances including a global parameterization for mixed layer baroclinic instability that improves the mixed layer characteristics and global overturning (Fox-Kemper et al. 2011), global observational estimates of the impact of submesoscale processes on restratification (Johnson et al. 2016), and observational estimates of the regional impact of a range of submesoscale processes on the seasonal cycle in the North Atlantic (Thompson et al. 2016). While these approaches are useful to advance our understanding, they do not fully account for variability of background conditions or include interactions between multiple submesoscale processes. The second approach has used regional and global models that partially resolve the submesoscale to suggest that submesoscale processes may have a global impact by helping to set surface heat fluxes (Barkan et al. 2017; Su et al. 2018), and by modulating deep water formation rates (Tagklis et al. 2020). However, these models do not fully resolve submesoscale processes (Fox-Kemper et al. 2019; Dong et al. 2020; Freilich et al. 2023), and therefore may not include smaller-scale processes associated with the submesoscale flows. While all these approaches of understanding cross-scale interactions between submesoscale fronts and the global scale are important steps, studies are needed that include all relevant scales and processes to gain a comprehensive characterization of the coupling between submesoscale and global scales.

In this study we use global observations of submesoscale density fronts to explore how their dynamics vary with large-scale properties in the surface ocean. We calculate submesoscale frontal buoyancy gradients using a global dataset of ship-based temperature and salinity observations to understand the factors that set the globally-averaged dynamics and geographic variability of submesoscale density fronts. The cross-front surface buoyancy gradient is defined as $b_x = M^2 = g\rho_x/\rho_o$ where b is the buoyancy, g is gravity, ρ is surface density, and ρ_o is the reference density of 1025 kg m^{-3}. We refer to fronts with a large b_x as being sharp. This new approach is valuable because the horizontal buoyancy gradients are directly related to frontal dynamics and have consequences for a wide range of processes associated with submesoscale fronts. For example, the buoyancy gradient scales with frontal width in a manner consistent with the underlying assumptions of quasi-geostrophic theory (see Section 2). Additionally, the frontal buoyancy gradient is a useful metric since it is related to the kinetic energy if one assumes geostrophic balance via $KE_g = (1/2)(Hb_x/f)^2$, where H is the mixed layer depth and f is the Coriolis frequency. The effective vertical heat fluxes due to the overturning caused by mixed layer baroclinic instability (Fox-Kemper et al. 2008) and Ekman (Thomas and Lee 2005) also scale with the frontal buoyancy gradient.

In the following we will first discuss a general scaling based on a subset of assumptions underlying quasi-geostrophic theory that will be used here as a framework to diagnose the statistically prevalent global submesoscale frontal dynamics (Section 2). A new method of identifying fronts using ship-based observations and determining frontal orientation using satellite SST data is then presented (Section 3 and 4). Finally, we will show that the frontal buoyancy gradient scales with the frontal width, as expected from some of the underlying assumptions of quasi-geostrophy, and explore what sets the geographic variability of the submesoscale frontal buoyancy gradients (Section 5) and discuss how these results can be interpreted in the context of previous work that has focused on local submesoscale processes and the evolution of regional submesoscale flows (Section 6).

2. Scaling

Many studies focus on the distribution of energy across scales as a means of diagnosing whether interior quasi-geostrophic dynamics (Charney 1971) or alternative theories (e.g., surface quasi-geostrophy) play a dominant role in shaping the submesoscale field in the upper ocean, and thus the direction of the energy cascade (Callies and Ferrari 2013; Rocha et al. 2016; Qiu et al. 2017; Chereskin et al. 2019). When techniques are applied to separate the internal waves from the balanced flow (Bühler et al. 2014), submesoscales of ∼10-40 km have been shown to have kinetic energy spectral slopes of -3 that are consistent with interior quasigeostrophy in Drake Passage (Rocha et al. 2016), shallower -2 slopes that are expected from other theories (e.g., surface quasigeostrophy) in the California Current and the North Equatorial Current/Countercurrent (Qiu et al. 2017; Chereskin et al. 2019), and slopes between these two extremes in the Kuroshio Current (Qiu et al. 2017). Due to data resolution limitations, very few studies have focused on the smaller end of the submesoscale range (1-10 km). One such study produces results that suggest (with numerous caveats) that geostrophic dynamics may be important on scales as small as 1-20 km, depending on the season, in the Gulf of Mexico (Balwada et al. 2022). While this collection of studies provides insight into submesoscale dynamics and indicates variability between regions, it also has limitations since it has primarily targeted scales larger than the mixed layer deformation radius and it diagnoses submesoscale dynamics by making strong assumptions to remove internal waves.

Here we take a different approach to diagnosing the prevalent dynamics of the observed submesoscale density fronts: we compare the frontal buoyancy gradient to a scaling based on some of the assumptions underlying quasi-geostrophic theory. The scaling is built from the Rossby number $Ro = U/fL$, and the Froude number $Fr = U/NH$, where U is the characteristic frontal velocity, L is the characteristic frontal length-scale (half the frontal width), and N is the buoyancy frequency within the mixed layer. Here we assume that $Fr \sim Ro$ or, equivalently, that that the Burger Number $Bu = (Ro/Fr)^2 \sim 1$. Note that this assumption can be combined with the additional assumption that $Ro \ll 1$ to form the interior quasi-geostrophic equations (Charney 1971), which have been shown to be consistent with observations of the submesoscale in some regions (e.g., Rocha et al. 2016). The quasi-geostrophic assumptions can be combined with additional assumptions (e.g., that potential vorticity is zero in the interior) to form the surface quasi-geostrophic equations (Held et al. 1995), which have been used to describe submesoscale dynamics in other studies (LaCasce and Mahadevan 2006; Lapeyre and Klein 2006; Lapeyre 2017).

To relate the horizontal frontal buoyancy gradient b_x to L, we introduce the balanced Richardson number $Ri = N^2 f^2/M^4$, where $M^2 = b_x$. Combining the relation $Fr \sim Ro$, and Ri results in a scaling relating the frontal length scale to the horizontal buoyancy gradient,

$$b_x = M^2 = \frac{Lf^2}{\sqrt{Ri}H}. \tag{1}$$

The $b_x \sim L$ portion of this scaling was also found in Chen and Young (1995) for fronts when advection (e.g., due to mesoscale straining) is balanced by across-front nonlinear diffusion given by the subinertial mixed layer approximation (Young 1994). In this study we will assume that the balanced Ri is, on average, scale invariant across the ~1-10 km frontal widths we are considering. We argue that this is a reasonable assumption since previous theoretical work shows that $N^2 \sim M^4/f^2$ during submesoscale restratification (Tandon and Garrett 1995) and in the subinertial mixed layer approximation (Young 1994). We leave it to future work to justify this assumption over a wider range of conditions.

A different scaling than Equation 1 might be observed if the dominant dynamics of submesoscale fronts followed theoretical frameworks other than quasi-geostrophy. For example, if the ageostrophic terms were more important on average than is assumed in quasi-geostrophy, semi-geostrophic dynamics may be more appropriate as commonly described for a specific frontal orientation in (Hoskins 1974), and in a more general form can be shown to assume that $Fr \sim \sqrt{Ro}$ (Cullen 2006), which would lead to a different scaling than is presented in Equation 1.

3. Data

a. Ship Thermosalinograph Measurements

We use an updated version of the dataset described by Drushka et al. (2019), which consists of global observations of near-surface temperature and salinity collected from ships. Measurements were taken using thermosalinographs that were installed on a variety of research vessels, sailing vessels, and ships of opportunity at 5-10 m depth, considered here to represent the ocean surface. Collectively these vessels have sampled much of the ice-free global ocean, though the majority of coverage is in the North Pacific and North Atlantic and concentrated in shipping lanes. The dataset combines measurements from numerous databases that have been merged (with duplicates removed). Measurements were typically recorded every 1-5 minutes, resulting in horizontal resolution of 0.1 to 1.5 km at typical ship speeds of 2 to 5 m s^{-1}. A rigorous quality-control method was applied to remove spurious data (see Drushka et al. 2019, for details). The updated dataset extends from 1990 to 2020 and consists of over 32 million points following the quality control process.

b. Satellite Sea Surface Temperature

Level 2P global satellite SST data from the Group for High Resolution Sea Surface Temperature (GHRSST) Moderate-resolution Imaging Spectroradiometer (MODIS) Aqua, which has approximately 1 km resolution, is used in this study. This satellite SST data is available from July 2002 to present. Here we select only data that has a quality level of 3 ‘acceptable quality’ or higher to remove the impact of clouds.

4. Methods

a. Calculating the Submesoscale Frontal Buoyancy Gradients

To prepare the thermosalinograph data for submesoscale frontal identification, continuous and relatively straight segments are selected from the full dataset. The first step is to remove data that satisfies any of the following: (1) the previous data point was taken more than an hour before, (2) the angle between the position of the datapoint and the previous datapoint, or the two data points surrounding it, exceeds $\pi/10$, (3) the distance between a datapoint and the previous one exceeds 3 km, (4) the ship was moving less than 4 m/hr. After this process is complete, the ship tracks are divided into segments at least 20 km in length and of at least 20 datapoints. Next, each segment is subject to additional quality control including smoothing 'steppy' salinity segments (caused by rounding of the salinity data to 0.01 precision) with a 5-point Hanning filter, removing salinity spikes (defined as differing more than 2 standard deviations from a 7-point running mean), and discarding segments where salinity spikes are present in more than 1/50 of the datapoints. The absolute salinity, conservative temperature, and in situ density are then calculated and used in the remainder of the study (referred to as salinity, temperature, and density).

Submesoscale fronts are defined here as strings of at least four consecutive datapoints where the density gradient between each datapoint exceeds 0.01 kg /km^2 and has the same sign (See Figure 1 for an example). To account for remaining small spikes in the data (due to either data quality or physics), single outliers are allowed if the density gradient between the two points after the outlier is $\leq$ 0.01 kg/km^2 and has the same sign as remainder of the front. The density gradient for each front is calculated using a linear fit of all the points in the front. Fronts were discarded if the gradient from the fit was $\leq$ 0.01 kg/km^2 or if the associated r^2 was <0.5. This series of quality control checks is chosen to minimize the false-positive frontal identifications, with the trade-off of preferentially selecting narrower fronts; this therefore impacts quantities such as the distributions of frontal widths and buoyancy gradients. To account for this, here we focus on spatial variability and report quantitative results as a function of frontal width. The front identification process yields over 250,000 submesoscale fronts.

Due to the variety of possible angles between a given front and ship track as it crossed the front, the true frontal width will differ from the frontal width measured along the ship track. To account for this, the frontal width and density gradient is corrected using two approaches: (A) a statistical correction accounting for the mean offset due to the ships crossing fronts at a variety of angles, and (B) a satellite-based correction which includes the frontal orientation data calculated from satellite SST. Note, we do not need to account for aliasing due to frontal movement while the ship crosses the front because the effect is negligible since this study considers averages of a large number of fronts.

The first step in the statistical correction approach (A) assumes that both the ship tracks and the frontal orientations are randomly distributed. The frontal width in the ship reference frame w_s is related to the width of the front in earth coordinates w_e, by $w_e = w_s cos(\theta)$, where θ is the smallest angle between the ship track and the front. We can therefore approximate the frontal width in Earth coordinates w_e, $w_e = w_s|cos(\theta)|$ where $||$ denotes the mean. We assume a random distribution of fronts and ship tracks so that $|cos(\theta)| = 2/\pi$.

Near coasts the statistical correction has a propensity to underestimate the frontal width since fronts tends to run parallel to coastlines (Mauzole 2022) and ship tracks are preferentially perpendicular to coasts. For all data within 250 km of a coastline, an additional empirical correction is applied to compensate. The distance from the closest coast was determined using 1 m resolution bathymetry data (v18 of Smith and Sandwell 1997). A correction c was then chosen so that close to coasts $w_e = cw_s|cos(\theta)|$, where $c = 1 - cos(\pi/4(d(1/250 + 1))$ and d is the distance from the coast, which increases buoyancy gradients close to the coasts by a factor of 2-3. Applying this correction improves mean estimates of the buoyancy gradient close to the coasts, so that they are more closely aligned with Approach (B), the satellite-corrected buoyancy gradients.

In addition to the statistical correction, an independent estimate of the frontal width is generated by applying a satellite-based correction (B) to each front that overlaps with satellite SST data. The satellite-based correction is made by matching each front with GHRSST MODIS Aqua satellite SST data, and using this match to calculate the front's orientation, and its associated width and density gradient. First, satellite SST data is identified that overlaps spatially with a ship-based segment and is within 1 day of the in situ data. As a first quality control check to see if the observed fronts are aligned with the satellite data, a linear regression plane fit is applied to the satellite SST data averaged within 2 km of each shiptrack frontal datapoint. Fronts for which the sign of the

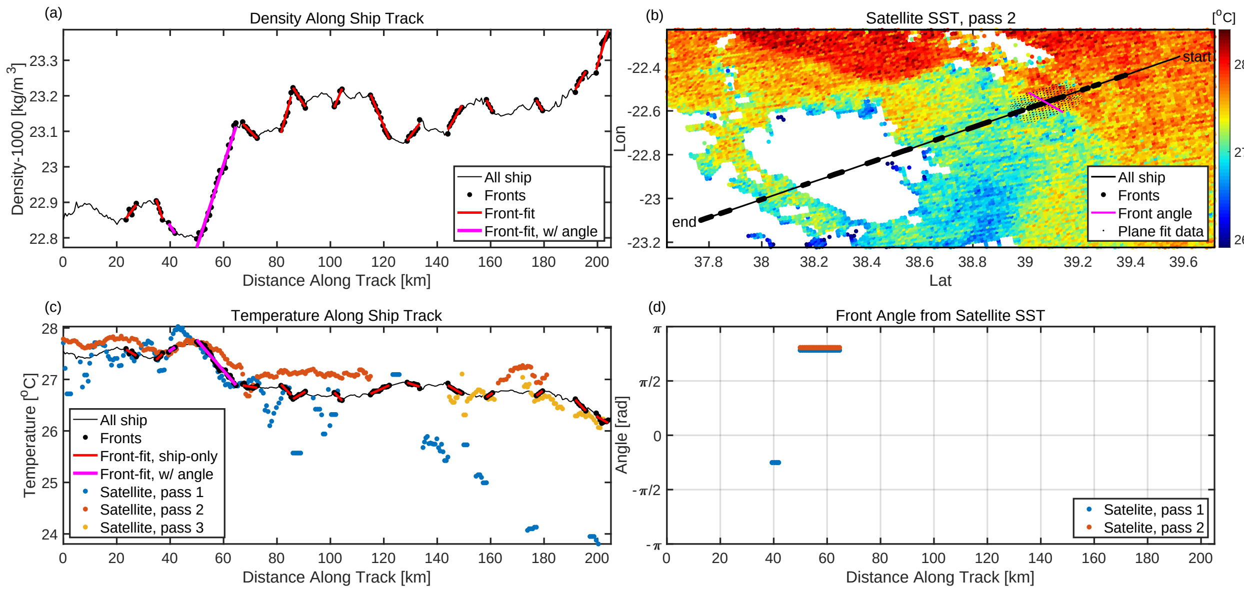

FIG. 1. An example implementation of the front detection method. (a) Density along a ship track, with data points used determined to be part of fronts (black dots), and fit frontal gradients (lines), including those with (pink), and without (red) satellite angle estimates. (b) Satellite sea surface temperature (SST) for pass 2, with shiptrack (black line), and frontal locations (large black dots), front angle (pink line), and data used for the plane fit (small black dots). White regions are clouds. (c) The same as (a), except for temperature and with the addition of satellite SST data along the shiptrack. (d) The calculated frontal angles from each satellite pass.

fit did not agree with the in situ frontal gradient sign are discarded at this stage for computational efficiency.

Next, to obtain satellite data used to find the frontal orientation, for each in situ datapoint in each front, satellite data are selected that are close to the fronts (at most 1/2 the width of the front away, as observed from the ship). Fronts are then discarded that have too few satellite data points associated with them, with the requirement that the number of data points both exceeds 5 and exceeds 1/2 the frontal width squared as measured from the ship. For fronts with sufficient satellite data, a plane was fit to the satellite SST data to determine the orientation of the front.

Planar regression is commonly used to fit planes to data, where a r^2 value is a measure of goodness of fit. Since the satellite SST data has frequent gaps (e.g., due to cloud cover), planar regression was not used since a r^2 value does not account for poor fits due to the common issue of spatially clustered or linear data distributions. Instead, we use the moment of inertia method (Fernández 2005; Woodcock 1977) to find the plane fit of the satellite SST data, which finds the best-fit plane where the vector normal to the plane is the equivalent to the maximum moment of inertia if the data points had mass. Using this method, the degree to which the satellite data is orientated in a line as opposed to a cluster, as measured by $K = ln(\lambda_1/\lambda_2)/ln(\lambda_2/\lambda_3)$, where λ are the eigenvalues of the inertia matrix (See Fernández (2005); Woodcock (1977) for details). Here we require that $K \geq 0.5$ and $r^2 \geq 0.3$ to use the estimate of the frontal orientation obtained from satellite data. The moment of inertia method plane fit is used to calculate the orientation of the front to the ship track, and to produce an estimate of the width and density gradient associated with each front in Earth coordinates. Approximately 1/10 of identified fronts have a satellite-based estimate of frontal width and gradient.

In the year 2015, a total of 219 fronts had multiple satellite crossings and thus multiple angles of the front could be compared to check the robustness of the satellite-based method. If the difference between the angles is measured on a scale from 0 to π, a total of 59% of fronts agreed within $\pi/4$ and a total of 87% of fronts agreed within $\pi/2$ which is good agreement given that fronts may move within the 1 day time window required to match satellite and ship-track data.

The frontal buoyancy gradient b_x is then calculated by combining the observed frontal widths with the observed density gradients by using both the corrected ship-based method and satellite method for rotating the fronts into Earth coordinates. The probability density functions of the frontal widths and horizontal buoyancy gradients are similar using both methods (Figure 2a and b). If the ship-frame widths and buoyancy gradients are subsampled to include only fronts that also have satellite-based estimates, the discrepancy between the two probability density functions is reduced, indicating that a portion of the difference is due to differences in spatial sampling. Figure 2c shows the joint probability density function of the frontal width and the buoyancy gradient for the ship-based method. The mean frontal buoyancy gradient as a function of frontal width is poorly resolved for fronts smaller than 1.5 km due to shiptrack data resolution limitations and frontal selection choices. Due to this, the remainder of this study focuses on submesoscale fronts larger than 1.5 km in width. Additionally, the upper limit for frontal width for the majority of

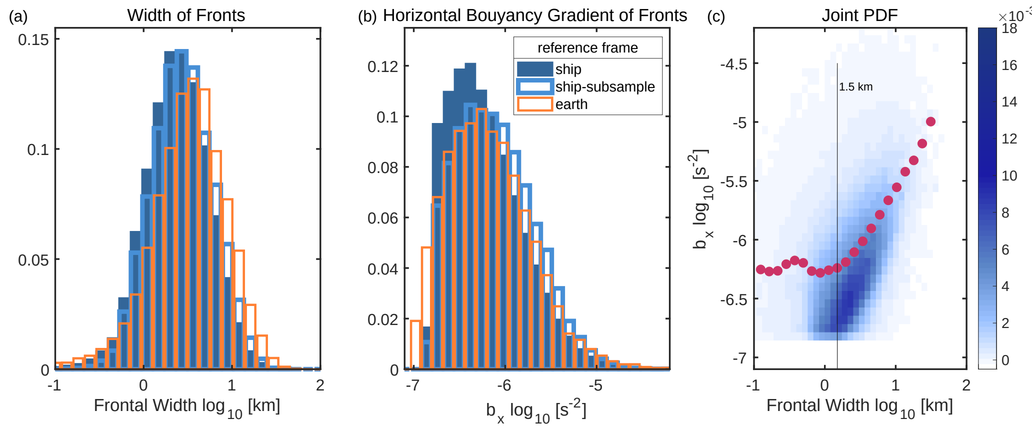

FIG. 2. The probability density distributions of the (a) widths and (b) buoyancy gradients of the observed submesoscale fronts. Filled blue bars indicate frontal characteristics that are calculated in ship coordinates, empty orange bars indicate that they are calculated in Earth coordinates using satellite data, and empty light blue bars indicate that variables are calculated in ship coordinates but subsampled for the fronts that have concurrent satellite data. (c) The joint probability density function of the frontal width and buoyancy gradients in ship coordinates with the mean buoyancy gradients for given frontal widths are indicated by magenta dots.

figures is 30 km, with the exception of the maps, which have an upper cut-off of 10 km to avoid the less common large gradients associated with wider fronts appearing as spatial variability.

b. Mixed Layer Depth and Buoyancy Frequency

The mixed layer depth and buoyancy frequency are estimated using over 1.3 million temperature, salinity, and pressure profiles from the global Argo dataset between 2011 and 2023 (Figure 4). For each Argo profile the mixed layer depth is calculated using the variable density threshold method (de Boyer Montegut et al. 2004), where the mixed layer depth is defined as the depth where the density is equal to the density at 10 m plus a density equivalent to a 0.2°C increase from the properties at 10 m.

The buoyancy frequency throughout the mixed layer is very low, with an increase near the mixed layer base, and therefore the mean buoyancy frequency within the mixed layer can be sensitive to the definition of the mixed layer depth. To account for this, we define the mixed layer buoyancy frequency as the mean in the upper 3/4 of the mixed layer. As a measure of error, the mixed layer

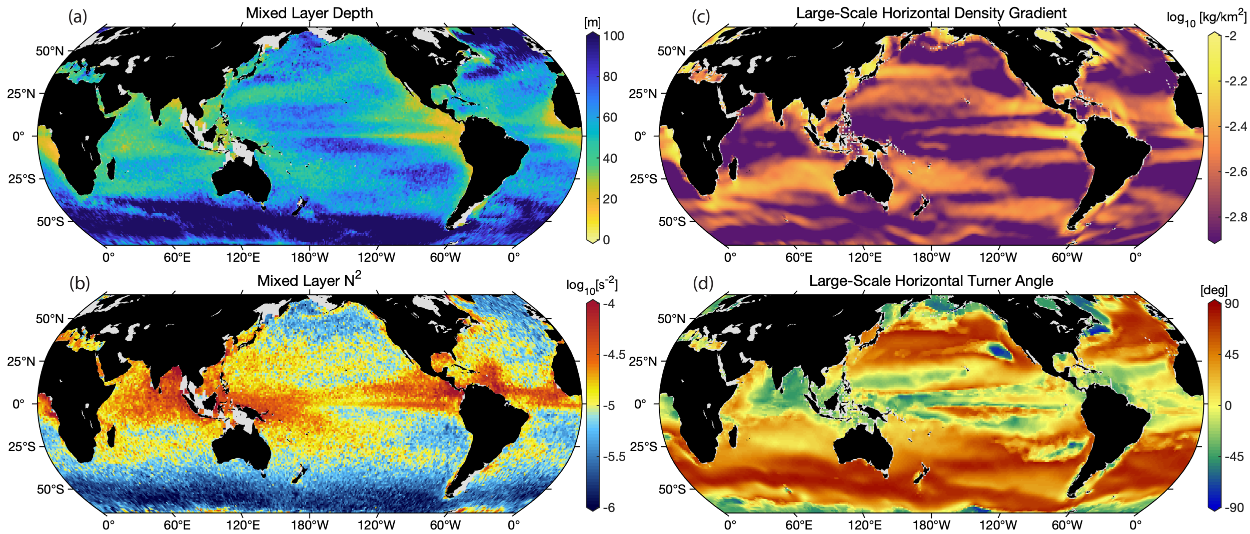

FIG. 3. Full year averages of monthly products of the (a) average mixed layer depth, (b) average mixed layer buoyancy frequency, (c) large-scale horizontal density gradient, and (d) large-scale horizontal Turner angle. The mixed layer depth and buoyancy frequency are both calculated from Argo float data. The horizontal density gradient and Turner angle are both calculated from the World Ocean Atlas climatology.

buoyancy frequency is also calculated by changing the averaging range to the full mixed layer depth and 1/2 the mixed layer depth. Globally, the mixed layer buoyancy frequency increases as the mixed layer shallows (Figure 4), which is similar to the trend shown by Dong et al. (2020) calculated by applying a slightly different method to Argo data from only the months of August and February. A global 1° monthly product of the mean mixed layer depth and mixed layer buoyancy frequency was constructed (Figure 3c, d). As expected due to the impact of averaging, the maximum mixed layer buoyancy frequency for shallow mixed layers is smaller for the product than that of the individual Argo profiles (Figure 4). Note that the climatologies of mixed layer depth and mixed layer buoyancy frequency is only an approximation of the across-front properties, and therefore have associated uncertainties when these variables are used to calculate quantities such as the balanced Richardson number.

c. Large-Scale Horizontal Density Gradient and Turner Angle

The monthly World Ocean Atlas sea surface temperature and salinity, which have 1 degree resolution, are used to calculate the large-scale horizontal density gradient and Turner angle. The

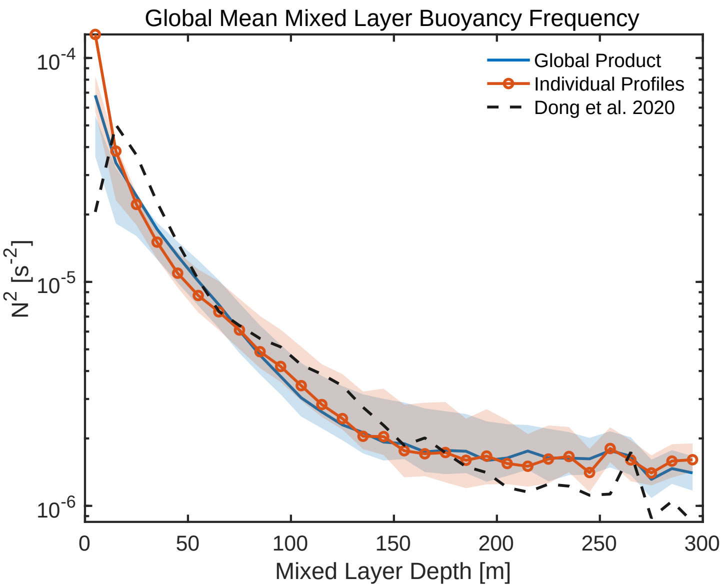

FIG. 4. The mean mixed layer buoyancy frequency is elevated where the mixed layer is shallower, as calculated using values from individual Argo profiles (orange circles and lines) and a monthly product of monthly means calculated from the Argo measurements (blue line). The lines are the average mixed layer buoyancy frequency over the upper 3/4 of the mixed layer, and the shaded regions are bounded by the mean mixed layer buoyancy frequency when the buoyancy frequency is averaged over the upper 1/2 or full mixed layer depth. The mixed layer buoyancy frequency from Dong et al. (2020) calculated using a different approach and only incorporating data from August and February has a similar trend (dotted black line).

annual-mean of the monthly products of both quantities are shown in Figure 3c and d, respectively. The large-scale horizontal Turner angle is calculated following Johnson et al. (2012)

$$Tu_h = arctan\left(\frac{\nabla\rho \bullet (\alpha\nabla T + \beta\nabla S)}{\nabla\rho \bullet (\alpha\nabla T - \beta\nabla S)}\right),$$

where the density gradient $\nabla\rho$, temperature gradient ∇T, and salinity gradient ∇S are all vectors and α is the thermal expansion coefficient and β is the haline contraction coefficient. Here we use the inverse tangent defined on the interval from -90° to 90°. Positive angles indicate the

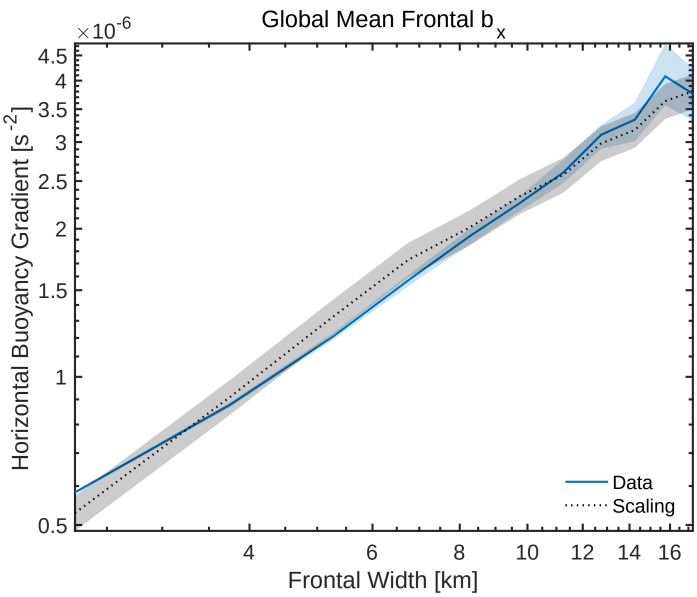

FIG. 5. The mean frontal buoyancy gradient as a function of frontal width for fronts using ship-based observations (solid) where confidence intervals are 90% bootstrapped. The scaling (dotted) is shown for $b_x = Lf/(\sqrt{Ri}H)$ where H is calculated from Argo data and the balanced Richardson number is fit to 0.9±0.1. The error bars delineate the high and low bounds when the scaling fit to the 90% bootstrapped confidence intervals of the data.

density gradient is temperature-dominated, and negative angles indicate the density gradient is salinity-dominated.

5. Results

The global distribution of submesoscale fronts, including their horizontal cross-front buoyancy gradient and associated frontal width, is presented here, focusing on fronts 1.5-30 km wide. Each submesoscale front is co-located with the monthly mean mixed layer depth, mixed layer buoyancy frequency, large-scale horizontal buoyancy gradient, and large-scale horizontal Turner angle. The following explores the dominant dynamics governing the observed submesoscale fronts globally and how these dynamics vary geographically and are modulated by background mixed layer characteristics.

In the global mean, the cross-front buoyancy gradient scales with the frontal width, where wider fronts are associated with sharper frontal buoyancy gradients (Figure 5). Here we compare the observed scale dependence of the mean frontal buoyancy gradient with the scaling $b_x = Lf^2/(\sqrt{Ri}H)$ (Equation 1), where L is twice the observed frontal width and H is the mixed layer depth from climatology. The balanced Richardson number, Ri, is then estimated by bin averaging, followed by applying a least-squares fit to find the y-intercept in log space. We find that a balanced Richardson number of 0.9±0.1 fits the data globally, which is consistent with a Richardson number of $O(1)$ expected in submesoscale flows when thermal wind is assumed (e.g. Thomas et al. 2008). The observed magnitude of the balanced Richardson number implies that globally the observed mean submesoscale fronts tend towards stability (smaller Richardson numbers are associated with a range of instabilities (Thomas et al. 2013)). Additionally, since the slope of the observed frontal buoyancy gradient matches Equation 1, the results suggest that, on average, the observed fronts are consistent with the underlying assumptions of the scaling (i.e., consistent with some assumptions of quasigeostrophy).

Global maps of the observed mean submesoscale frontal buoyancy gradients show variability of over an order of magnitude, typically ranging between $10^{-7}s^{-2}$ and $3x10^{-6}s^{-2}$ (Figure 6). Larger buoyancy gradients are found close to the coasts, in strong current systems (e.g., in western boundary current extensions), near river outflows (e.g., the Amazon), and in eastern upwelling systems (e.g., off the coast of northwest Africa and western Australia). There are many similarities between the geography observed here and the persistent SST fronts mapped globally by Mauzole (2022). For example, strong current systems and eastern upwelling systems have both numerous persistent SST fronts and sharper (larger b_x) submesoscale density fronts, as shown in Figure 6. The regional variability of frontal sharpness implies that submesoscale frontal dynamics have distinct dominant characteristics in different regions of the world.

There are seasonal differences between the distribution of submesoscale frontal horizontal buoyancy gradients (Figure 6), which are consistent with regional studies. For example, previous work found that the Amazon River plume is located mainly along the coast north of the river outlet from February through June, and has a 30% chance of migrating to middle of the basin, approximately between 50-30W, between May and September (Coles et al. 2013). These previous findings are consistent with the location and seasonal cycle of the frontal buoyancy gradient sharpness shown

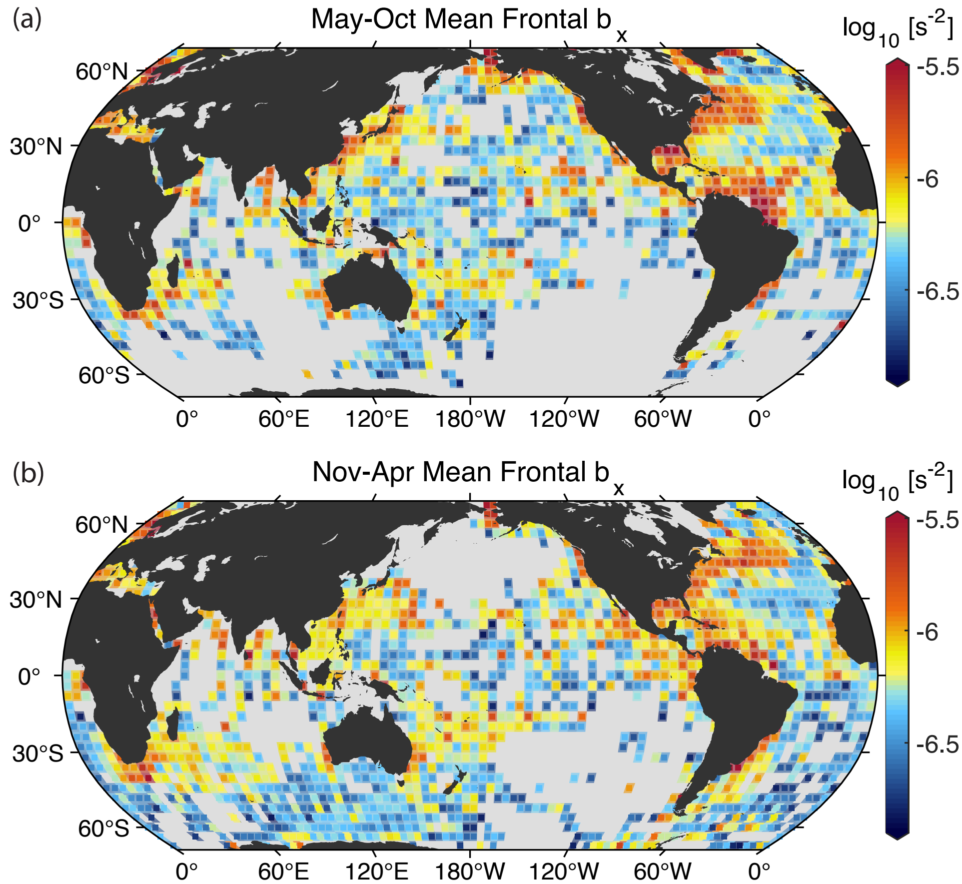

FIG. 6. Global mean submesoscale frontal buoyancy gradient from ship-based data averaged between (a) May-October and (b) November-April.

in Figure 6. Another example is near the coastline of the northeastern tropical Pacific, where the horizontal buoyancy gradients are elevated in the winter months compared to the summer months. Gaps in the mountains create strong localized winds during the winter months that blow over the Gulf of Tehuantepec, Papagayo, and Panama, cooling the sea surface and generating submesoscale features hundreds of kilometers from the coast (Liang et al. 2009), the signature of which is apparent in Figure 6.

On average, sharper buoyancy gradients at submesoscale fronts are found where the large-scale background density gradient is also large (Figure 7a). The correlation between submesoscale and background large-scale gradients holds globally for both submesoscale frontal gradients calculated in Earth coordinates using satellite data, and gradients using ship-based data only. Since the ship-based frontal dataset is large, it can be divided into 20° latitudinal bands, revealing a correlation

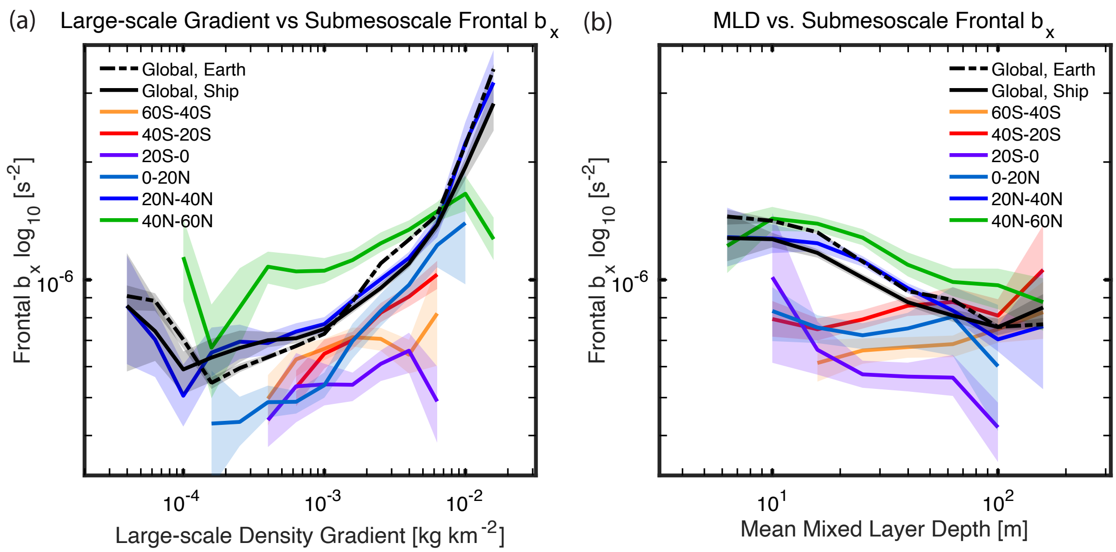

FIG. 7. Mean submesoscale frontal horizontal buoyancy gradients as a function of the (a) large-scale density gradient and (b) mixed layer depth. The global mean in Earth coordinates (black, dashed), global mean in ship coordinates (black, solid), and latitude-band average in ship coordinates (colors, solid). Means of over 200 fronts are plotted and uncertainty is estimated with 90% bootstrapped confidence intervals.

in all bands. While the trends in the Northern Hemisphere are consistently significant, in the Southern Hemisphere the correlation is not always significant, which may be due to the role of rough topography in driving submesoscale activity in the Antarctic Circumpolar Current (Dove et al. 2022) or the relative paucity of data.

For a given large-scale density gradient, submesoscale fronts are typically sharper when the large-scale horizontal Turner Angle is negative, corresponding to large-scale gradients that are dominated by salinity as opposed to temperature (Figure 8). The sharpest fronts globally occur when $\mathrm{Tu}_h < -\pi/8$ and the large-scale density gradient is $> 10^{-3}$ kg/km^2. For example, some of the sharpest submesoscale fronts occur near the Amazon River outflow where the large-scale gradients are strongly dominated by salinity. In contrast, the central North Pacific at mid-latitudes has strongly temperature-dominated large-scale lateral gradients and have only moderately sharp submesoscale fronts.

Shallow mixed layers are globally correlated with larger submesoscale frontal buoyancy gradients, calculated in either the ship or Earth reference frame (Figure 7b). Additionally, sharper frontal buoyancy gradients are found where the mixed layer is shallow for all individual latitude bands

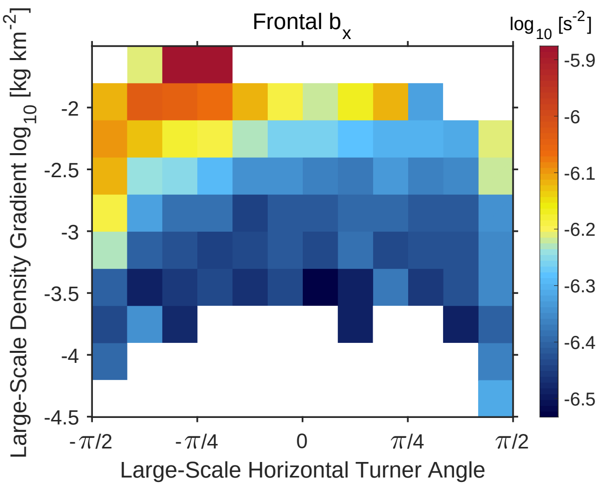

FIG. 8. The median buoyancy gradient across submesoscale fronts as a function of the large-scale horizontal density gradient and large-scale horizontal Turner angle. A minimum of 25 fronts are require to plot a bin.

except for in the mid-latitude Southern Hemisphere and the Southern Ocean (60-20°S). The global negative correlation between the frontal buoyancy gradient and mixed layer depth is expected given the $1/H$ dependence in Equation 1. Note that the global correlation observed here between shallow mixed layer and sharp frontal buoyancy gradients, and the elevated submesoscale activity during spring restratification shown in previous work (e.g. Haine and Marshall 1998; Boccaletti et al. 2007; Fox-Kemper et al. 2008), can both occur simultaneously on different time and length scales as discussed in Section 6.

While on average the horizontal frontal buoyancy gradients are larger when the mixed layer is shallow, there is evidence that this is modulated by a secondary effect of the opposite sign. Where the mixed layer is shallow, the mixed layer buoyancy frequency tends to be larger (Figure 4), which increases the balanced Richardson number (Figure 9b). According to Equation 1, a larger balanced Richardson number would lead to relatively smaller values of b_x, modulating the main $1/H$ influence of mixed layer depth on b_x. Evidence that this modulation occurs can be found by estimating the balanced Richardson number by calculating a scaling fit analogous to that in Figure 2, modified so that it is applied over a variety of mixed layer depth ranges (See Figure 9a for an example with three ranges). We find that the fit-based balanced Richardson number is larger when the mixed layer is shallow, and varies over an order of magnitude (Figure 9b).

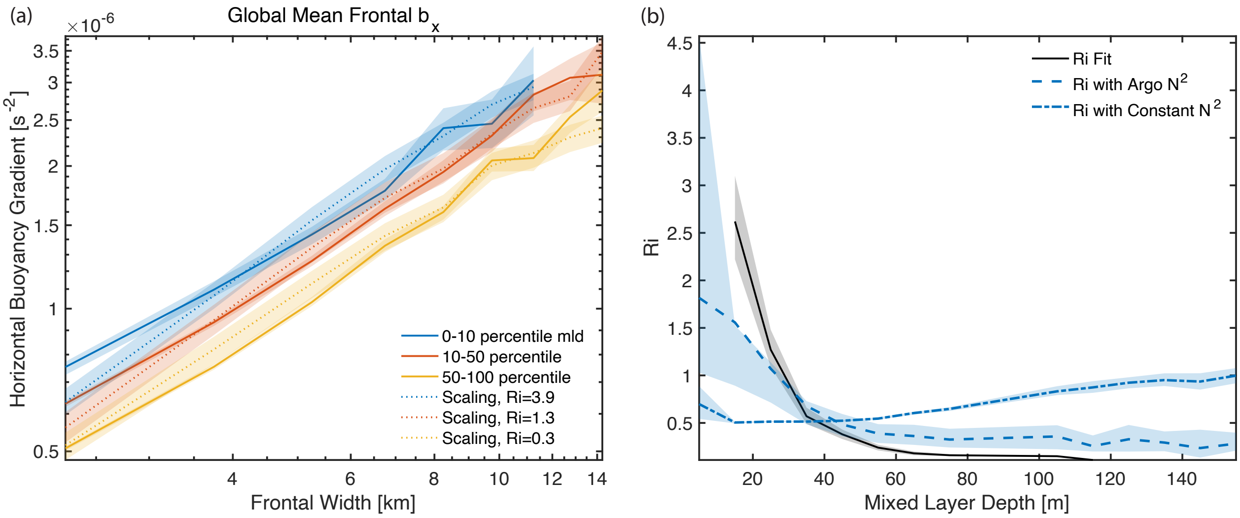

FIG. 9. The variability of the balanced Richardson number with mixed layer depth, calculated either using a fit or using Argo data. (a) Identical to Figure 5, except that the fronts are divided according to mixed layer depth percentile, the 0-10th percentile (0-17 m), 10-50th percentile (17-34 m), and 50-100th percentile (>34 m), and the balanced Richardson number fit is done for each percentile group (see Figure 5 for details). (b) The balanced Richardson number calculated using buoyancy frequency from Argo data and ship-based horizontal buoyancy gradients (blue, dashed) with 90% bootstrapped confidence intervals calculated using the mean buoyancy frequencies in the upper one half or full mixed layer; scaling fit and confidence intervals calculated as in Figure 5, but for each mixed layer depth bin (black, solid); and a constant buoyancy frequency of 4.6x$10^{-3}s^{-1}$, which is the mean; and ship-based horizontal buoyancy gradients (blue, dotted) with 90% bootstrapped confidence intervals.

The fit-based balanced Richardson number as a function of mixed layer depth closely tracks the balanced Richardson number calculated from Argo data (Figure 9b). In contrast, there is little agreement when a constant mixed layer buoyancy frequency is used to calculate the balanced Richardson number (Figure 9b). In summary, the result here suggests that in addition to the main correlation described above between shallower mixed layers and sharper buoyancy gradients (the $1/H$ effect), there is an opposite, modulating effect of larger balanced Richardson number (the $1/\sqrt{Ri}$ in Equation 1) due to larger mixed layer buoyancy frequencies in shallower mixed layers. As a word of caution, note that concurrent measurements of mixed layer depth and frontal gradients are needed over a wide range of background conditions to fully test and confirm the role of the balanced Richardson number suggested by these observations.

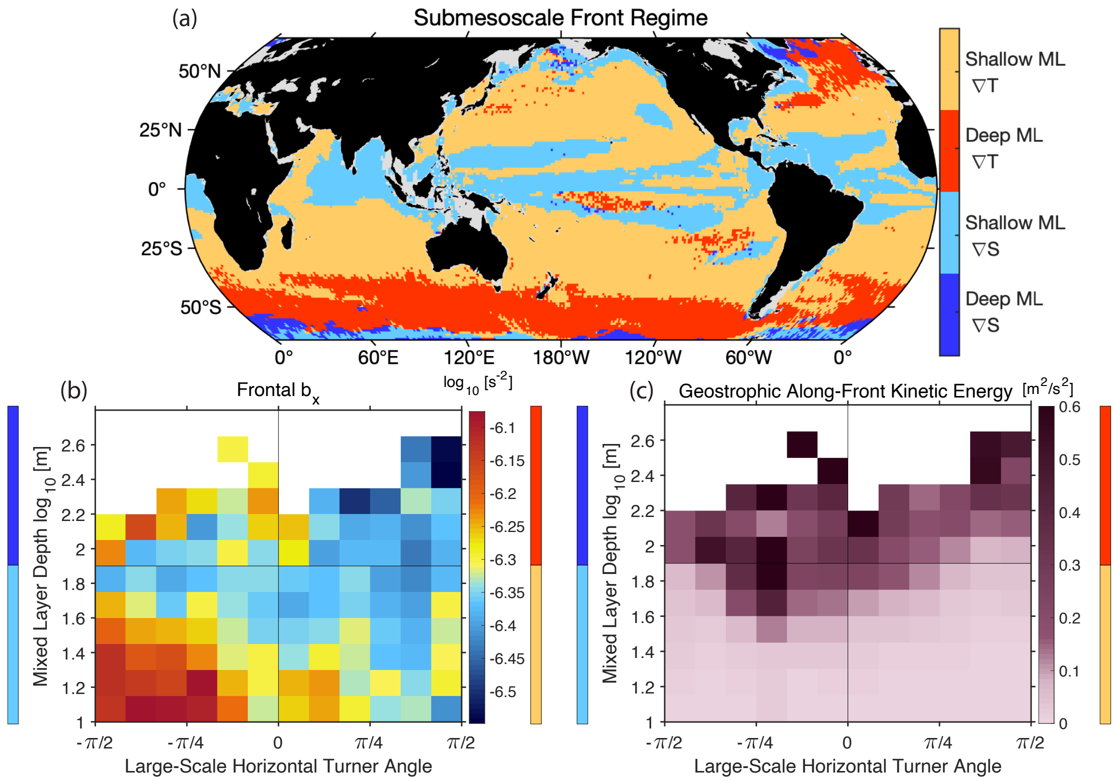

FIG. 10. Four regimes of submesoscale frontal dynamics, shown in (a) including a shallow mixed layer and $0<\mathrm{Tu}_h$ (dark yellow), deep mixed layer and $0<\mathrm{Tu}_h$ (red), shallow mixed layer and $\mathrm{Tu}_h<0$ (light blue), deep mixed layer and $\mathrm{Tu}_h<0$ (dark blue). A deep mixed layer is defined as >80m, and $0<\mathrm{Tu}_h$ indicates that the large-scale density gradient is temperature-dominated whereas $\mathrm{Tu}_h<0$ indicates that it is salinity-dominated. (b) The median submesoscale frontal buoyancy gradient or (c) the geostrophic frontal kinetic energy, as a function of the large-scale Turner angle and the mixed layer depth. Lines delineate the four regimes, which are also shown as the colors corresponding to the colorbar in (a).

To better appreciate the dual impact of the mixed layer depth (MLD) and the large-scale horizontal Turner angle, the ocean can be divided into four regimes by separating regions into negative vs. positive Turner angle, and shallow vs. deep mixed layers. Figure 10b shows the submesoscale buoyancy gradients associated with each regime and Figure 10a designates the spatial extent of each regime on a global map. The sharpest frontal submesoscale buoyancy gradients (median b_x is 5.6x10^{-7} s^{-2}) occur where the mixed layer is shallow and the large-scale gradients are salinity-dominated (MLD<80 m, $\mathrm{Tu}_h<0$). These regions include coastal areas where there is a large amount of freshwater outflow from rivers (e.g., the Ganges and the Amazon) and in the tropical rain bands and monsoon-influenced regions where there is large freshwater input from rain, consistent with previous studies that have found uncompensated, salinity-dominated submesoscale density variability in these regions (MacKinnon et al. 2016; Spiro Jaeger and Mahadevan 2018; Drushka et al. 2019). In regions where the mixed layer is shallow and large-scale density gradient is dominated by temperature (MLD<80 m, 0<Tu$_h$), submesoscale horizontal buoyancy gradients tend to be moderate (median b_x is 4.5x10^{-7} s^{-2}). This regime is predominately in the center of each basin in the mid-latitudes. Next, we move on to the regime where the mixed layer is deep and the large-scale gradients are salinity dominated (80 m<MLD, Tu$_h$ <0), which has moderate frontal buoyancy gradients (median b_x is 4.9x10^{-7} s^{-2}). This regime occurs less frequently and is predominately confined to high latitudes away from coasts where there is surface freshwater input from precipitation and glacial and sea ice melt (e.g. in the Southern Oecan, Haumann et al. 2016) as well as outflow of fresh Arctic waters (in the North Atlantic, Haine et al. 2015). Finally, the frontal buoyancy gradients are the smallest (median b_x is 4x10$^{-7}s^{-2}$) in the final regime where the mixed layer is deep and the large-scale density gradients are dominated by temperature (80 m<MLD, 0<Tu$_h$). This regime typically occurs far from coasts at high latitudes such as the Southern Ocean and the subpolar Atlantic.

Other metrics of submesoscale frontal dynamics also vary globally. For example, the frontal kinetic energy, estimated here by assuming that each front is in geostrophic balance, $KE_g = 1/2(Hb_x/f)^2$, on average varies according to the mixed layer depth and the large-scale horizontal Turner angle (Figure 10c). When the mixed layer is deeper the submesoscale fronts have more geostrophic kinetic energy. Interestingly, for a given mixed layer depth, the kinetic energy is larger when the large-scale gradient is dominated by salinity (Tu$_h$ <0) due to the tendency for sharper submesoscale fronts when the large-scale gradient is dominated by salinity.

6. Discussion

This study explores a global dataset of submesoscale density fronts to understand their governing dynamics, geographic distribution, and linkages to a range of background characteristics, including the mixed layer depth, mixed layer buoyancy frequency, large-scale horizontal gradients, and large-scale horizontal Turner angle. We find that the global mean submesoscale frontal buoyancy gradients scale with the frontal width following a relationship that is consistent with theory, and also vary geographically in correlation with the background large-scale environment.

In their entirety, these results provide a link between submesoscale fronts and the large-scale characteristics and dynamics of the surface mixed layer. Our interpretation is that the large-scale background variables described here help set the sharpness of submesoscale density fronts on large spatial scales and long timescales. On smaller scales, a variety of previously explored mechanisms then modulate the submesoscale frontal gradient sharpness, including processes that eliminate strong frontal density gradients by facilitating frontal compensation (Young 1994; Rudnick and Ferrari 1999; Spiro Jaeger and Mahadevan 2018), seasonal variability of surface buoyancy forcing that generates submesoscale instabilities (Haine and Marshall 1998; Boccaletti et al. 2007), and mesoscale straining (McWilliams 2016). Therefore, we would expect that the submesoscale frontal dynamics are a consequence of interactions on a range of scales including both local processes and the average background properties. In a mean sense, the submesoscale frontal processes then feedback to help to set the large-scale properties of the surface ocean through a variety of mechanisms that are currently under active research (Taylor and Thompson 2023).

Globally, the observed mean submesoscale dynamics scale with frontal width (Figure 5) according to Equation 1, which assumes the balance $Fr \sim Ro$. The implication is that submesoscale fronts 1.5-10 km wide scale according to *some* of the assumptions underlying quasigeostrophy, as opposed to alternative dynamics such as semigeostrophy, which would require $Fr \sim \sqrt{Ro}$ (Cullen 2006). Unlike the full set of quasigeostrophic assumptions, here we do not include direct constraints on the magnitude of Ro. Note that the result is valid for a global average, indicating that a range of dominant dynamics is possible among the observed fronts, which could include fronts that have strong ageostrophic components. Consequently, studies that focus on strongly ageostrophic individual submesoscale features (e.g. Freilich et al. 2023) or fronts subject to symmetric instability (Thomas et al. 2013), may be highlighting a subset of the range of possible submesoscale dynamics. Our findings also begin to extend the knowledge of dynamics to smaller scales within the submesoscale range compared to previous work, which has focused on scales larger than the mixed layer deformation radius and has found evidence for quasigeostrophic dynamics in a number of different regions (Rocha et al. 2016; Qiu et al. 2017; Chereskin et al. 2019), however more work is needed to fully understand the dynamics of these smaller submesoscales.

Our results show that submesoscale frontal gradients tend to be sharper when the large-scale horizontal density gradient is large (Figure 8), especially when the gradient is salinity-dominated (Tu_h <0) as opposed to temperature-dominated (0<Tu_h), suggesting that gradients on the large scale play a role in setting those on the submesoscale. Sharp fronts where the background density gradient is large may be due to a combination of effects including (1) the stirring of large-scale density gradients could generate sharper submesoscale fronts, and (2) kinetic energy associated with large background density gradients could aid in forming sharp submesoscale fronts. The observation that sharper fronts occur where the background gradient is salinity-dominated as opposed to temperature-dominated suggests that cross-scale coupling is modulated by different processes in each case. Possible contributing factors include (1) the role of air-sea fluxes on frontal dynamics in regions where the large-scale gradient is salinity- versus temperature-dominated (e.g. Spiro Jaeger and Mahadevan 2018); (2) an elevated mixed layer buoyancy frequency, and therefore more stable balanced Richardson number, in salinity-dominated regions (Figure 3b,d); or (3) differences in boundary conditions between the two regimes (e.g., gradients are sustained differently in the case of river plumes as opposed to western boundary current extensions). We leave it to future work to fully investigate these potential mechanisms.

Throughout the global ocean, we find that sharper submesoscale buoyancy gradients are correlated with shallower mixed layers (Figure 7b), consistent with what is expected from Equation 1. Much of the previous work highlighting the link between mixed layer depth and submesoscale activity has found that the submesoscale is more active when a deep mixed layer is shoaling during springtime restratification due to heightened mixed layer baroclinic instability (e.g. Callies et al. 2015; Thompson et al. 2016; Yu et al. 2019). To reconcile these two results, we suggest that the equilibrium dynamics (represented in Equation 1) may cause sharper fronts when the mixed layer is shallow globally, while local transient processes such as mixed layer restratification can temporarily cause elevated submesoscale activity as the potential energy in deep mixed layers is converted to kinetic energy in submesoscale fronts and eddies. Our results suggest that equilibrium dynamics may be more important than mixed layer restratification processes in setting the correlation between mixed layer depth and frontal sharpness on a global scale. An additional consideration is that models do not currently resolve the smallest submesoscale features associated with a shallow mixed layer during the warmer months (Dong et al. 2020), suggesting that higher-resolution modeling is needed to fully understand the seasonal cycle of submesoscale activity and how it is related to mixed layer depth.

The global-mean balanced Richardson number associated with submesoscale density fronts observed here is 0.9±0.1, consistent with $O1$ Richardson number found during theoretical studies of restratification (Tandon and Garrett 1995) and the subinertial mixed layer approximation (Young 1994). Geographically, the balanced Richardson number associated with submesoscale fronts varies over an order of magnitude between regions with deep mixed layers and shallow mixed layers in part due to changes in the mixed layer buoyancy frequency (Figure 9), which according to Equation 1 could cause a modulating effect of the opposite sign impacting the magnitude of submesoscale buoyancy gradients. These results imply that the coupling between vertical mixing processes and submesoscale dynamics, which has been studied in specific contexts (Hamlington et al. 2014; Whitt and Taylor 2017; Callies and Ferrari 2018), is important globally. Additionally, our results suggest that submesoscale fronts are, on average, more stable to processes such as symmetric instability and mixed layer baroclinic instability when the mixed layer is shallow due to a larger mean balanced Richardson number. Future studies are needed that include concurrent mixed layer depth and vertical/horizontal buoyancy gradient measurements to fully understand the linkages between turbulent mixing in the mixed layer, the balanced Richardson number, and submesoscale fronts globally.

Our results predominately focus on the frontal horizontal buoyancy gradient as an indicator of submesoscale dynamics, and briefly show how the results relate to another characterization of submesoscale dynamics, the total geostrophic kinetic energy (Figure 10c). In this example, sharper frontal buoyancy gradients in regions of salinity-dominated background density gradients ($\mathrm{Tu}_h < 0$) also cause elevated total geostrophic kinetic energy compared to regions with temperature-dominated background gradients with the same mixed layer depth. This suggests that submesoscale frontal dynamics vary between these two regimes, but also cross-scale energy fluxes and interactions between vertical mixing processes and the submesoscale may also have distinctly different characteristics in the two regimes. Similarly, the global variability of submesoscale dynamics may have important impacts on quantities such as carbon export or equivalent heat flux due to submesoscale instabilities, opening a number of possible avenues for future work.

7. Conclusion

The observations here demonstrate that submesoscale frontal buoyancy gradients vary globally as a function of frontal width according to the scaling $b_x = Lf^2/(\sqrt{Ri}H)$. The frontal buoyancy gradients also vary geographically with the large-scale density gradient, large-scale horizontal Turner angle, and mixed layer depth in a way suggesting that the balanced Richardson number is also important for setting the geographic variability of frontal dynamics on a global scale. Notably, we find that globally shallower mixed layers are associated with sharper submesoscale fronts, which has not be described in previous work.

The majority of previous studies concerning submesoscale dynamics have focused on explaining the evolution of fronts due to transient local processes such as surface buoyancy forcing and mesoscale straining, or the balance of vertical mixing processes on the frontal scale. Our study takes a different approach by applying a global observational perspective to focus on mean dynamics and the role of background properties in altering submesoscale fronts. This global-scale perspective is important since frontal dynamics are known to impact the global-scale air-sea interactions, buoyancy fluxes, across-scale energy transfers, carbon export, and productivity, and therefore studying the complementary influence of the large scale on the small scale is critical for completeness. We view this work as a first step on this global trajectory and hope it inspires future theory, modeling, and observational studies to fully explore and explain the global patterns these observations reveal.

Acknowledgments. This work was supported by NASA-PO grants 80NSSC18K0776 and 80NSSC19K1116. The authors thank Peter Gaube for helpful discussions and comments on an version of this manuscript.

Data availability statement. The compiled thermosalinograph data used in this study is available for download (https://zenodo.org/records/12584849). The Level 2 satellite SST data from GHRSST MODIS Aqua is freely available on NASA PODAAC (https://doi.org/10.5067/GHMDA-2PJ02). The Argo float data used here were collected and made freely available by the International Argo Program and the national programs that contribute to it (https://argo.ucsd.edu, https://www.ocean-ops.org). The Argo Program is part of the Global Ocean Observing System. The 2018 World Ocean Atlas data is freely available for download (https://www.ncei.noaa.gov/products/world-ocean-atlas).

References

Balwada, D., J.-H. Xie, R. Marino, and F. Feraco, 2022: Direct observational evidence of an oceanic dual kinetic energy cascade and its seasonality. *Science Advances*, **8 (41)**, eabq2566.

Barkan, R., J. C. McWilliams, A. F. Shchepetkin, M. J. Molemaker, L. Renault, A. Bracco, and J. Choi, 2017: Submesoscale dynamics in the northern gulf of mexico. part i: Regional and seasonal characterization and the role of river outflow. *Journal of Physical Oceanography*, **47 (9)**, 2325–2346.

Boccaletti, G., R. Ferrari, and B. Fox-Kemper, 2007: Mixed layer instabilities and restratification. *J. Phys. Oceanogr.*, **37 (9)**, 2228–2250.

Bühler, O., J. Callies, and R. Ferrari, 2014: Wave–vortex decomposition of one-dimensional ship-track data. *J. Fluid Mech.*, **756**, 1007–1026.

Callies, J., and R. Ferrari, 2013: Interpreting energy and tracer spectra of upper-ocean turbulence in the submesoscale range (1–200 km). *J. Phys. Oceanogr.*, **43 (11)**, 2456–2474.

Callies, J., and R. Ferrari, 2018: Baroclinic instability in the presence of convection. *Journal of Physical Oceanography*, **48 (1)**, 45–60.

Callies, J., R. Ferrari, J. M. Klymak, and J. Gula, 2015: Seasonality in submesoscale turbulence. *Nat. Commun.*, **6**.

Charney, J. G., 1971: Geostrophic turbulence. *Journal of the Atmospheric Sciences*, **28 (6)**, 1087–1095.

Chen, L., and W. Young, 1995: Density compensated thermohaline gradients and diapycnal fluxes in the mixed layer. *Journal of physical oceanography*, **25 (12)**, 3064–3075.

Chereskin, T. K., C. B. Rocha, S. T. Gille, D. Menemenlis, and M. Passaro, 2019: Characterizing the transition from balanced to unbalanced motions in the southern california current. *Journal of Geophysical Research: Oceans*, **124 (3)**, 2088–2109.

Coles, V. J., M. T. Brooks, J. Hopkins, M. R. Stukel, P. L. Yager, and R. R. Hood, 2013: The pathways and properties of the amazon river plume in the tropical north atlantic ocean. *Journal of Geophysical Research: Oceans*, **118 (12)**, 6894–6913.

Cullen, M. J. P., 2006: *A mathematical theory of large-scale atmosphere/ocean flow*. World Scientific.

D'Asaro, E., C. Lee, L. Rainville, R. Harcourt, and L. Thomas, 2011: Enhanced turbulence and energy dissipation at ocean fronts. *science*, **332 (6027)**, 318–322.

de Boyer Montegut, C., G. Madec, A. S. Fischer, A. Lazar, and D. Iudicone, 2004: Mixed layer depth over the global ocean: An examination of profile data and a profile-based climatology. *J. Geophys. Res.-Oceans*, **109 (C12)**.

Dong, J., B. Fox-Kemper, H. Zhang, and C. Dong, 2020: The seasonality of submesoscale energy production, content, and cascade. *Geophysical Research Letters*, **47 (6)**, e2020GL087 388.

Dove, L. A., D. Balwada, A. F. Thompson, and A. R. Gray, 2022: Enhanced ventilation in energetic regions of the antarctic circumpolar current. *Geophysical Research Letters*, **49 (13)**, e2021GL097 574.

Drushka, K., W. E. Asher, J. Sprintall, S. T. Gille, and C. Hoang, 2019: Global patterns of submesoscale surface salinity variability. *Journal of Physical Oceanography*, **49 (7)**, 1669–1685.

Fernández, O., 2005: Obtaining a best fitting plane through 3d georeferenced data. *Journal of Structural Geology*, **27 (5)**, 855–858.

Fox-Kemper, B., R. Ferrari, and R. Hallberg, 2008: Parameterization of mixed layer eddies. Part I: Theory and diagnosis. *J. Phys. Oceanogr.*, **38 (6)**, 1145–1165.

Fox-Kemper, B., and Coauthors, 2011: Parameterization of mixed layer eddies. III: Implementation and impact in global ocean climate simulations. *Ocean Modelling*, **39 (1)**, 61–78.

Fox-Kemper, B., and Coauthors, 2019: Challenges and prospects in ocean circulation models. *Frontiers in Marine Science*, **6**, 65.

Freilich, M., L. Lenain, and S. T. Gille, 2023: Characterizing the role of non-linear interactions in the transition to submesoscale dynamics at a dense filament. *Geophysical Research Letters*, **50 (15)**, e2023GL103 745.

Haine, T. W., and J. Marshall, 1998: Gravitational, symmetric, and baroclinic instability of the ocean mixed layer. *J. Phys. Oceanogr.*, **28 (4)**, 634–658.

Haine, T. W., and Coauthors, 2015: Arctic freshwater export: Status, mechanisms, and prospects. *Global and Planetary Change*, **125**, 13–35.

Hamlington, P. E., L. P. Van Roekel, B. Fox-Kemper, K. Julien, and G. P. Chini, 2014: Langmuir–submesoscale interactions: Descriptive analysis of multiscale frontal spindown simulations. *Journal of Physical Oceanography*, **44 (9)**, 2249–2272.

Haumann, F. A., N. Gruber, M. Münnich, I. Frenger, and S. Kern, 2016: Sea-ice transport driving southern ocean salinity and its recent trends. *Nature*, **537 (7618)**, 89–92.

Held, I. M., R. T. Pierrehumbert, S. T. Garner, and K. L. Swanson, 1995: Surface quasi-geostrophic dynamics. *Journal of Fluid Mechanics*, **282**, 1–20.

Hoskins, B., 1974: The role of potential vorticity in symmetric stability and instability. *Quarterly Journal of the Royal Meteorological Society*, **100 (425)**, 480–482.

Johnson, G. C., S. Schmidtko, and J. M. Lyman, 2012: Relative contributions of temperature and salinity to seasonal mixed layer density changes and horizontal density gradients. *Journal of Geophysical Research: Oceans*, **117 (C4)**.

Johnson, L., C. M. Lee, and E. A. D'Asaro, 2016: Global Estimates of Lateral Springtime Restratification. *J. Phys. Oceanogr.*, **46 (5)**, 1555–1573.

LaCasce, J. H., and A. Mahadevan, 2006: Estimating subsurface horizontal and vertical velocities from sea-surface temperature. *Journal of Marine Research*, **64 (5)**, 695–721.

Lapeyre, G., 2017: Surface quasi-geostrophy. *Fluids*, **2 (1)**, 7.

Lapeyre, G., and P. Klein, 2006: Dynamics of the upper oceanic layers in terms of surface quasigeostrophy theory. *J. Phys. Oceanogr.*, **36 (2)**, 165–176.

Liang, J.-H., J. C. McWilliams, and N. Gruber, 2009: High-frequency response of the ocean to mountain gap winds in the northeastern tropical pacific. *Journal of Geophysical Research: Oceans*, **114 (C12)**.

Liu, G., A. Bracco, and U. Passow, 2018: The influence of mesoscale and submesoscale circulation on sinking particles in the northern gulf of mexico. *Elementa: science of the Anthropocene*, **6**.

MacKinnon, J. A., and Coauthors, 2016: A tale of two spicy seas. *Oceanography*, **29 (2)**, 50–61.

Mahadevan, A., 2016: The impact of submesoscale physics on primary productivity of plankton. *Annu. Rev. Mar. Sci.*, **8**, 161–184.

Mauzole, Y., 2022: Objective delineation of persistent sst fronts based on global satellite observations. *Remote Sensing of Environment*, **269**, 112 798.

McWilliams, J. C., 2016: Submesoscale currents in the ocean. *Proceedings of the Royal Society A: Mathematical, Physical and Engineering Sciences*, **472 (2189)**, 20160 117.

Molemaker, M. J., J. C. McWilliams, and I. Yavneh, 2005: Baroclinic instability and loss of balance. *J. Phys. Oceanogr.*, **35 (9)**, 1505–1517.

Omand, M. M., E. A. D'Asaro, C. M. Lee, M. J. Perry, N. Briggs, I. Cetinić, and A. Mahadevan, 2015: Eddy-driven subduction exports particulate organic carbon from the spring bloom. *Science*, **348 (6231)**, 222–225.

Peng, J.-P., P. Holtermann, and L. Umlauf, 2020: Frontal instability and energy dissipation in a submesoscale upwelling filament. *Journal of Physical Oceanography*, **50 (7)**, 2017–2035.

Qiu, B., T. Nakano, S. Chen, and P. Klein, 2017: Submesoscale transition from geostrophic flows to internal waves in the northwestern pacific upper ocean. *Nature communications*, **8 (1)**, 1–10.

Rocha, C. B., T. K. Chereskin, S. T. Gille, and D. Menemenlis, 2016: Mesoscale to submesoscale wavenumber spectra in drake passage. *Journal of Physical Oceanography*, **46 (2)**, 601–620.

Rudnick, D. L., and R. Ferrari, 1999: Compensation of horizontal temperature and salinity gradients in the ocean mixed layer. *Science*, **283 (5401)**, 526–529.

Smith, W. H. F., and D. T. Sandwell, 1997: Global sea floor topography from satellite altimetry and ship depth soundings. *Science*, **277**, 1956–1962.

Spiro Jaeger, G., and A. Mahadevan, 2018: Submesoscale-selective compensation of fronts in a salinity-stratified ocean. *Science advances*, **4 (2)**, e1701 504.

Su, Z., J. Wang, P. Klein, A. F. Thompson, and D. Menemenlis, 2018: Ocean submesoscales as a key component of the global heat budget. *Nature communications*, **9 (1)**, 1–8.

Tagklis, F., A. Bracco, T. Ito, and R. Castelao, 2020: Submesoscale modulation of deep water formation in the labrador sea. *Scientific reports*, **10 (1)**, 17 489.

Tandon, A., and C. Garrett, 1995: Geostrophic adjustment and restratification of a mixed layer with horizontal gradients above a stratified layer. *Journal of physical oceanography*, **25 (10)**, 2229–2241.

Taylor, J. R., and A. F. Thompson, 2023: Submesoscale dynamics in the upper ocean. *Annual Review of Fluid Mechanics*, **55**, 103–127.

Thomas, L. N., and C. M. Lee, 2005: Intensification of ocean fronts by down-front winds. *J. Phys. Oceanogr.*, **35 (6)**, 1086–1102.

Thomas, L. N., A. Tandon, and A. Mahadevan, 2008: Submesoscale processes and dynamics. *Ocean modeling in an Eddying Regime*, 17–38.

Thomas, L. N., J. R. Taylor, R. Ferrari, and T. M. Joyce, 2013: Symmetric instability in the Gulf Stream. *Deep Sea Res. Part II Top. Stud. Oceanogr.*, **91**, 96–110.

Thompson, A. F., A. Lazar, C. Buckingham, A. C. Naveira Garabato, G. M. Damerell, and K. J. Heywood, 2016: Open-ocean submesoscale motions: A full seasonal cycle of mixed layer instabilities from gliders. *J. Phys. Oceanogr.*, **46 (4)**, 1285–1307.

Whitt, D. B., and J. R. Taylor, 2017: Energetic submesoscales maintain strong mixed layer stratification during an autumn storm. *Journal of Physical Oceanography*, **47 (10)**, 2419–2427.

Woodcock, N., 1977: Specification of fabric shapes using an eigenvalue method. *Geological Society of America Bulletin*, **88 (9)**, 1231–1236.

Young, W., 1994: The subinertial mixed layer approximation. *Journal of physical oceanography*, **24 (8)**, 1812–1826.

Yu, X., A. C. Naveira Garabato, A. P. Martin, C. E. Buckingham, L. Brannigan, and Z. Su, 2019: An annual cycle of submesoscale vertical flow and restratification in the upper ocean. *Journal of Physical Oceanography*, **49 (6)**, 1439–1461.